Article

Structural and Thermoelectric Properties of $Gd_{2-2x}Sr_{1+2x}Mn_2O_7$ Double-Layered Manganites

Nailing Qin [1], Yehai Pang [1], Zhengbing Xu [1,2], Xiyong Chen [1,2] and Jialin Yan [1,2,*]

1 School of Resources, Environment and Materials, Guangxi University, Nanning 530004, China
2 State Key Laboratory of Featured Metal Materials and Life-Cycle Safety for Composite Structures, Nanning 530004, China
* Correspondence: yjl@gxu.edu.cn

Abstract: Double-layered manganites are natural superlattices with low thermal conductivity, which is of importance for potential thermoelectric applications. The $Gd_{2-2x}Sr_{1+2x}Mn_2O_7$ (x = 0.5; 0.625; 0.75) were prepared by the solid-state reaction method. All the samples crystallize in the tetragonal I4/mmm $Sr_3Ti_2O_7$ type structure. The unit cell volume and the distortion in the MnO_6 octahedra increase with increasing Gd content. Their thermoelectric properties were investigated between 300 and 1200 K. All exhibit an *n*-type semiconducting behavior. The electrical conductivity (σ) increases while the absolute value of the Seebeck coefficient ($|S|$) decreases with increasing Gd content. Simultaneous increases in σ and $|S|$ with increasing temperature are observed at temperatures approximately higher than 600 K, and the power factor reaches a maximum value of 18.36 $\mu W/(m\ K^2)$ for x = 0.75 at 1200 K. The thermal conductivity (κ) is lower than 2 W/(m K) over the temperature range of 300–1000 K for all the samples and a maximum dimensionless figure of merit ZT of 0.01 is obtained for x = 0.75 at 1000 K.

Keywords: double-layered manganites; crystal structure; thermoelectric properties; *n*-type perovskite oxides

1. Introduction

Since the report of the layered $NaCo_2O_4$ showing good thermoelectric (TE) performance with a large Seebeck coefficient of 100 $\mu V/K$ at 300 K [1], there has been increasing interest in exploring new oxide TE materials in the last two decades because of their high chemical and thermal stability at high temperature, low toxicity, and relatively low-cost starting materials [2,3]. TE materials enable the direct conversion of thermal into electricity and are useful for manufacturing TE devices for power generation from waste heat. The efficiency of a TE material is mainly determined by the dimensionless figure of merit ZT, which is a product of the TE figure of merit Z and the absolute temperature T, given by $ZT = S^2\sigma T/\kappa$, where S, σ, κ, and T are the Seebeck coefficient, electrical conductivity, thermal conductivity, and absolute temperature, respectively. A good TE material requires large S, high σ, and low κ. As these three parameters are strongly coupled, depending on the carrier concentration and electronic structure, and there is a trade-off between S and σ, it is difficult to enhance them simultaneously. The power factor PF, defined as $S^2\sigma$, is related to the electrical properties of a material. Whilst the performance of most TE oxides is limited by their low ZT values due to low PF and high κ, several layer-structured oxides show outstanding TE properties, such as *p*-type layered cobaltites $Ca_3Co_4O_9$ and BiCuSeO, and *n*-type perovskite oxides $CaMnO_3$ manganates and $SrTiO_3$ titanates [2–4]. Methods to enhance ZT mostly include doping, carrier engineering, defect chemistry engineering, nanostructuring/nanocomposites, band engineering, etc., aiming to improve PF and reduce κ [2,3,5–7].

The Ruddlesden–Popper (RP) compounds with a general formula $A_{m+1}B_mO_{3m+1}$ (A = rare earth (RE) and/or alkaline earth elements and B = transition metals) or $AO(ABO_3)_m$

have a natural superlattice structure consisting of an alternate stacking of multiple (*m*) perovskite structure BO_2 layers and a single rock-salt A_2O_2 layer along the *c* axis direction [8]. The double-layered oxides $A_3B_2O_7$ belong to the *m* = 2 member and the perovskites ABO_3 correspond to the *m* = ∞ member of the RP family. The layered structure of the RP compounds would enhance the phonon scattering at the interfaces between the A_2O_2 layer and perovskite layer and consequently reduce *κ*, which is of great importance for TE materials. Investigation on thermal conductivity in the thin films of the *m* = 1–5 and 10 members of the $(SrTiO_3)_mSrO$ RP superlattices showed that the *m* = 2 member had the lowest *κ* in this RP homologous series [9]. Significant reduction of *κ* values was observed in the layered $(Sr_{1-x}RE_x)_{m+1}Ti_mO_{3m+1}$ (*m* = 1, 2) [10] and $La_{2-2x}Ca_{1+2x}Mn_2O_7$ (0.75 ≤ *x* ≤ 1.0) [11] due to the intrinsic superlattice structure as compared to their perovskite phases. It is desired for a TE material that good electron transport properties *PF* would be kept while *κ* is reduced. The structure of the RP oxides allows compositional tailoring, and the TE properties of *n*-type $CaMnO_3$ and $SrTiO_3$ can be improved by substitution at either the A or B sites. It has been found that RE element doping at Ca sites of $CaMnO_3$ is an effective way to increase *σ* while keeping a moderate absolute *S* [6,12]. Studies of the effects of various RE^{3+} ions doping at Sr sites of $(Sr_{0.95}RE_{0.05})_3Ti_2O_7$ oxides on their TE properties indicated that the maximum *ZT* was obtained in Gd-doped $(Sr_{0.95}Gd_{0.05})_3Ti_2O_7$ mainly owing to its lower *κ* [13] or enhanced *S* [14].

The double-layered manganites $RE_{2-2x}Sr_{1+2x}Mn_2O_7$ are of significant interest due to the effect of colossal magnetoresistance (CMR) and intensive studies have been focused on their magnetic and magneto-transport properties [15–21]. However, works on the high-temperature TE properties of $RE_{2-2x}Sr_{1+2x}Mn_2O_7$ to take advantage of their intrinsic superlattice structures are very scarce. During the course of our systematic research on the phase diagram of the Gd–Sr–Co/Mn–O systems [22,23], a $Gd_{2-2x}Sr_{1+2x}Mn_2O_7$ solid solution was found. Our magnetic measurements of the $Gd_{2-2x}Sr_{1+2x}Mn_2O_7$ samples in the temperature range of 2–350 K under an applied magnetic field of 0.02 T show two ferromagnetic transitions, which is in analogy to the temperature-dependent magnetizations of $La_{1.2}Sr_{1.8}Mn_2O_7$ [24] and $La_{1.4}Sr_{1.6}Mn_2O_7$ [25]. In this paper, we report the structural and TE properties of double-layered manganites $Gd_{2-2x}Sr_{1+2x}Mn_2O_7$ (*x* = 0.5, 0.625, 0.75). Investigation on their TE properties revealed an *n*-type semiconducting behavior and a *κ* of lower than 2 W/(m K) over the temperature range of 300–1000 K. *σ* increases while the absolute value of *S* decreases with increasing Gd content.

2. Materials and Methods

Polycrystalline samples of $Gd_{2-2x}Sr_{1+2x}Mn_2O_7$ (*x* = 0.5, 0.625, 0.75) were prepared by the conventional solid-state reaction method in air. Gd_2O_3 (99.95%, Sinopharm, Beijing, China), $SrCO_3$ (≥99.0%, Sinopharm, Beijing, China), and $MnCO_3$ (99.95%, Aladdin, Shanghai, China) were used as starting materials. Gd_2O_3 and $SrCO_3$ were dried at 773 K for 24 h, and $MnCO_3$ at 373 K for 24 h prior to use. Stoichiometric amounts of the preheated powders were thoroughly mixed and ball-milled in anhydrous ethanol medium for 10 h in the agate grinding jars using a planetary ball mill (QM−3SP4, Nanjing, China). The resultant powders were calcined at 1123 K for 24 h in a muffle furnace. Subsequently, the calcined powders were reground, pressed into pellets with diameters of 15 mm and a thickness of ~4 mm or pressed into 20 mm long rectangular samples with widths of 4 mm and a thickness of ~3 mm, and sintered at 1673 K for 120 h.

Powder X-ray diffraction (XRD) data were collected on an x-ray diffractometer (Rigaku D/Max 2500V, Tokyo, Japan) using Cu *Kα* radiation over the angular range of 10° to 110° 2*θ*, with a step size of 0.02°. The XRD data were analyzed with the Rietveld method using the Fullprof program [26]. The microstructure of the sintered samples was examined by a field emission scanning electron microscope (FE-SEM, Hitachi SU8020, Tokyo, Japan) using the secondary electron (SE) mode. The chemical compositions of the samples were determined by the equipped energy-dispersive X-ray spectrometer (EDS, Oxford X-MAX80, Oxford, UK). Specimens for the measurements of *σ* and *S* were prepared by grinding and polishing

the sintered rectangular samples into a typical dimension of 3.9 mm × 2.0 mm × 19.0 mm. All the surfaces of the specimens were carefully polished with SiC emery papers before measurement to ensure parallel ends. The temperature dependences of σ and S were measured on a multifunctional thermoelectric materials measurement system (Advance Riko ZEM-3M10, Yokohama, Japan) in the temperature range of 300–1200 K in a helium atmosphere. The specimen was placed vertically between the upper and lower Pt block electrodes in the infrared heating furnace, and two probes of the thermocouple were adjusted to attach to the longitudinal side of the specimen. *V-I* plot measurement was carried out to check whether the specimen was well contacted with the probes before the simultaneous measurements of σ and S. The thermal conductivity κ was calculated using the relationship $\kappa = DC_p d$, where D is the thermal diffusivity, C_P is the specific heat capacity and d is the bulk density. D was measured using the laser flash method (NETZSCH LFA 457, Selb, Germany) on disc specimens with diameters of 12.7 mm and a typical thickness of 1.5 mm. C_P was measured using differential scanning calorimetry (NETZSCH STA 449 F3, Selb, Germany) under an argon atmosphere up to 1000 K. The bulk density d of the sintered discs was determined by Archimedes' method (Shimadzu AUW220D, Kyoto, Japan).

3. Results and Discussion

3.1. Structural and Morphological Analysis

Figure 1a shows the powder XRD patterns of $Gd_{2-2x}Sr_{1+2x}Mn_2O_7$ ($x = 0.5, 0.625, 0.75$). All the diffraction peaks can be indexed in a tetragonal $Sr_3Ti_2O_7$ type structure with space group I4/mmm (No. 139). A typical Rietveld refinement pattern and the crystal structure for the sample $x = 0.625$ are demonstrated in Figure 1b. As seen from the structure, two stacked MnO_2 layers (i.e., double perovskite layers) form the quasi-two-dimensional (2D) magnetic layer (called bilayer). Two adjacent MnO_2 bilayers are separated by the (Gd, Sr)$_2O_2$ rock salt layers. The refined structural parameters, theoretical density (ρ_x), selected bond lengths, and reliability factors for $Gd_{2-2x}Sr_{1+2x}Mn_2O_7$ are summarized in Table 1. The measured bulk density d of the sintered samples and the relative density (% T. D.) are also given in Table 1. The relative density for all the samples is about 94%, indicating that the samples are of similar compactness.

According to the analysis from the neutron powder diffraction data [27], the Sr/RE ions occupy two Wyckoff sites, i.e., 2b (0, 0, 1/2) site in the 12-coordinate perovskite-like block and 4e (0, 0, z) site in the 9-coordinate rock salt layer. As seen in Figure 1b, each Gd^{3+}/Sr^{2+} ion is labeled by 2b or 4e to indicate its atomic Wyckoff position. Smaller RE ions such as Gd^{3+}, Tb^{3+}, Dy^{3+}, etc., were found to prefer the 4e site [27]. Refinements on the occupancies of Gd^{3+}/Sr^{2+} ions showed that they co-occupied the 2b and 4e sites with a higher occupation of Gd^{3+} ions at the 4e sites. The refined occupancies of Gd^{3+}/Sr^{2+} ions are given in Table 1. This is in agreement with the results of the refinement of $DySr_2Mn_2O_7$ [27] and $(Sr_{0.95}RE_{0.05})_3Ti_2O_7$ [14]. This preferential occupation of RE^{3+} ions at the 4e sites might be due to the smaller ionic radius differences between RE^{3+} ions and 9-coordinate Sr^{2+} (r = 1.31Å, coordination number (CN) = 9) as compared to 12-coordinate Sr^{2+} (r = 1.44Å, CN = 12) [14]. With increasing Gd content, the unit cell volume increases while the unit cell parameter a first increases and then decreases, and c shows the opposite variation with a. These size variations have been found for $Nd_{0.2}La_{1.8-2x}Sr_{1+2x}Mn_2O_7$ ($0.3 \leq x \leq 0.7$) [28], and can be attributed to the simultaneous occurrence of the substitution of Sr^{2+} (r = 1.31Å, CN = 9) ions with smaller Gd^{3+} ions (r = 1.107Å, CN = 9) and the conversion of Mn^{4+} (r = 0.53 Å, CN = 6) to larger Mn^{3+} (high spin, r = 0.645 Å, CN = 6) to maintain charge neutrality. It is therefore expected that the increasing amount of the Jahn–Teller active Mn^{3+} ions would lead to a stronger MnO_6 octahedral distortion with increasing Gd content in $Gd_{2-2x}Sr_{1+2x}Mn_2O_7$. The tolerance factor t describes the structural distortion, defined as $t = (\langle r_A \rangle + r_O)/\left[\sqrt{2}(\langle r_B \rangle + r_O)\right]$, where r_O is the ionic radius of the O ion and $\langle r_A \rangle$ and $\langle r_B \rangle$ are the mean radii of the ions at the A and B sites, respectively. With increasing Gd content, $\langle r_A \rangle$ decreases and $\langle r_B \rangle$ increases, a decreasing t is then obtained which confirms the enhancement of the structural distortion. Accordingly, the bond lengths of the apical

Mn–O1 bonds (Mn to the apical oxygen atom O1 shared between the two MnO_2 layers within a bilayer) and the in-plane Mn–O3 bonds (Mn to the equatorial oxygen atom O3 in the MnO_2 layers) vary oppositely, with the Mn–O1 bonds along the c axis showing a larger extent of variation. The bond lengths of the apical Mn–O2 bonds (Mn to the apical oxygen atom O2 in the $(Gd/Sr)_2O_2$ rock-salt layers) are longer than those of the apical Mn–O1 and in-plane Mn–O3 bonds, and are elongated with increasing Gd content, which indicates the enlargement of the interlayer Mn–Mn distances.
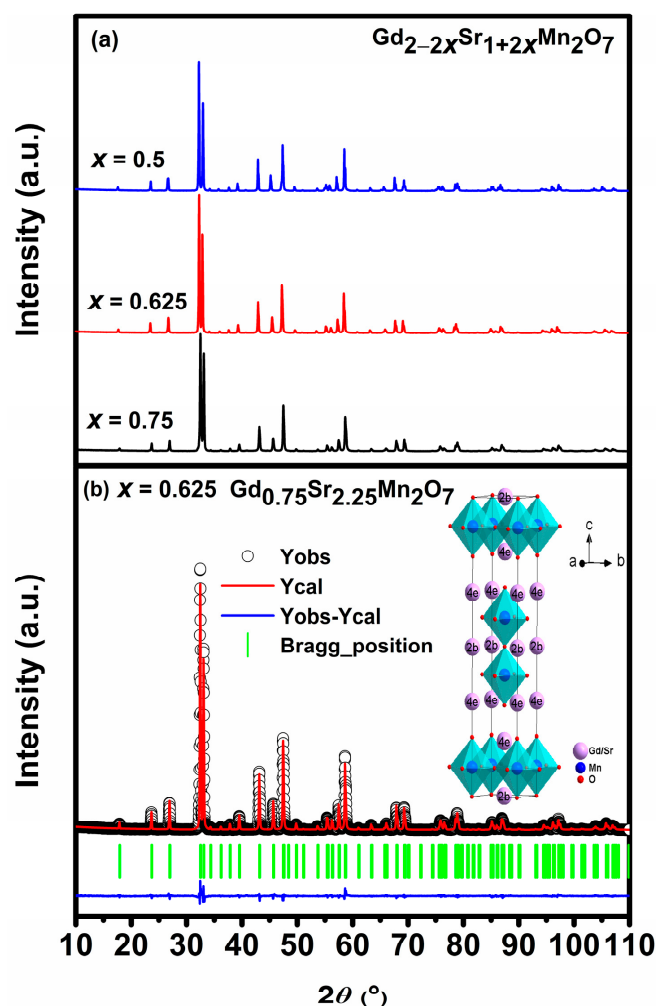

Figure 1. (**a**) Powder XRD patterns for $Gd_{2-2x}Sr_{1+2x}Mn_2O_7$ (x = 0.5, 0.625, 0.75). (**b**) Rietveld refinement pattern for x = 0.625. The inset shows the crystal structure of the unit cell.

Figure 2a–c presents the FE-SEM polished surface micrographs of sintered pellets of $Gd_{2-2x}Sr_{1+2x}Mn_2O_7$ (x = 0.5, 0.625, 0.75) samples. The insets of Figure 2a–c are the fractured surface micrographs. Samples x = 0.625 and x = 0.75 show similar polished surface morphologies, with an uneven surface and opened pores. It is evident from the insets that the fractured morphology evolves from slightly aggregated spherical shape grains for x = 0.5 to lath-like or even flake-shaped grains for x = 0.625 and x = 0.75, respectively. The fractured morphologies of all the samples show a dense structure, which is consistent with the relative density of 94% obtained from Archimedes' method (Table 1). Figure 2d shows the EDS mapping images of the cations for x = 0.625, indicating homogeneous distributions of the elements Gd, Sr, and Mn. The compositions measured by EDS are given in Table 2. It is shown that the molar ratios of the cations correspond well to the nominal compositions.

Table 1. Structural parameters obtained from Rietveld refinements for $Gd_{2-2x}Sr_{1+2x}Mn_2O_7$. Space group I4/mmm (No. 139), atomic Wyckoff positions: Gd1/Sr1, 2b (0, 0, 1/2), Gd2/Sr2, 4e (0, 0, z), Mn, 4e (0, 0, z), O1, 2a (0, 0, 0), O2, 4e (0, 0, z), O3, 8g (0, 1/2, z).

	x = 0.5	*x* = 0.625	*x* = 0.75
a (Å)	3.82705 (5)	3.83642 (7)	3.83446 (10)
c (Å)	20.0030 (3)	19.8882 (4)	19.9048 (6)
V (Å^3)	292.971 (7)	292.72 (1)	292.66 (1)
ρ_x (g/cm^3) *	6.342	6.123	5.842
d (g/cm^3)	5.9716	5.6942	5.5009
% T. D.	94.2	93.0	94.2
Occ. Gd1/Sr1	0.141/0.859	0.176/0.824	0.131/0.869
$z_{Gd2/Sr2}$	0.31729 (4)	0.31714 (4)	0.31677 (5)
Occ. Gd2/Sr2	0.466/0.534	0.306/0.694	0.150/0.850
z_{Mn}	0.09766 (8)	0.09698 (9)	0.0975 (1)
z_{O2}	0.1996 (3)	0.1973 (3)	0.1966 (4)
z_{O3}	0.0989 (2)	0.0969 (2)	0.0959 (3)
d_{Mn-O1} (Å)	1.9535 (18)	1.9288 (18)	1.9417 (24)
d_{Mn-O2} (Å)	2.0391 (63)	1.9952 (62)	1.9716 (83)
d_{Mn-O3} (Å)	1.9137 (1)	1.91821 (4)	1.9175 (1)
Rp (%)	10.9	10.7	12.8
Rwp (%)	12.7	12.7	15.2
Rexp (%)	7.38	7.09	6.69

* Calculated using the relationship $\rho_x = ZM/(N_A V)$, where *Z* is the number of formula units per unit cell, *M* is the sum of the atomic weights of all cations and all anions in the formula unit, N_A is Avogadro's number and *V* is the volume of the unit cell. Here *Z* = 2. *M* was calculated from the compositions obtained from the refined occupancies, not from the nominal compositions.
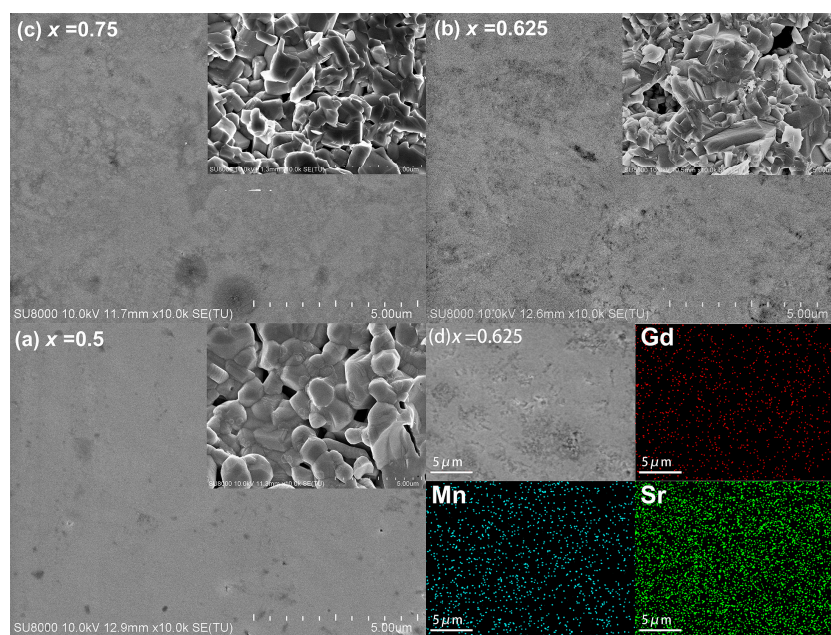

Figure 2. FE-SEM micrographs of the polished surface of sintered $Gd_{2-2x}Sr_{1+2x}Mn_2O_7$ with (**a**) *x* = 0.5, (**b**) *x* = 0.625, (**c**) *x* = 0.75. The insets of (**a**–**c**) are the fractured surface micrographs. (**d**) EDS mapping images for *x* = 0.625.

Table 2. The measured compositions from EDS results for $Gd_{2-2x}Sr_{1+2x}Mn_2O_7$ (*x* = 0.5, 0.625, 0.75).

x	Nominal Formula	EDS Composition (at.%)			EDS Formula
		Gd	Sr	Mn	
0.5	$GdSr_2Mn_2O_7$	20.77 ± 3.53	40.02 ± 1.48	39.21 ± 3.28	$Gd_{1.038}Sr_{2.001}Mn_{1.961}O_7$
0.625	$Gd_{0.75}Sr_{2.25}Mn_2O_7$	14.07 ± 4.12	46.25 ± 4.28	39.68 ± 1.92	$Gd_{0.703}Sr_{2.313}Mn_{1.984}O_7$
0.75	$Gd_{0.5}Sr_{2.5}Mn_2O_7$	12.64 ± 3.79	46.49 ± 3.67	40.87 ± 1.67	$Gd_{0.632}Sr_{2.325}Mn_{2.043}O_7$

3.2. Thermoelectric Properties

Figure 3a shows the temperature dependence of σ for $Gd_{2-2x}Sr_{1+2x}Mn_2O_7$ (x = 0.5, 0.625, 0.75) in the temperature range of 300–1200 K. All the samples exhibit a semiconducting behavior with $d\sigma/dT > 0$. σ increases gradually with increasing Gd content at the high-temperature region, and a maximum value of 6.1×10^3 S/m at 1200 K is observed for x = 0.5, which is of the same order of magnitude as those for $Ca_{0.96}Dy_{0.02}RE_{0.02}MnO_3$ [29]. As the substitution of Gd^{3+} ions for Sr^{2+} ions induces Mn^{3+} ions and donates electrons, where the nominal amount of Mn^{3+} ions (i.e., nominal electron concentration) can be estimated from the composition subscript ($2-2x$) while the nominal amount of Mn^{4+} ions (nominal hole concentration) estimated from the composition subscript ($2x$), the Jahn–Teller distortion of the Mn^{3+} ions leads to the formation of polarons where the electrons are localized due to the strong electron–phonon coupling. The electrical transport of $Gd_{2-2x}Sr_{1+2x}Mn_2O_7$ is thought to be dominated by the hopping motions of electrons or small polaron between Mn^{3+} and Mn^{4+} ions. The small polaron hopping conduction can be expressed by the equation [30]:

$$\sigma(T) = \frac{\sigma_0}{T} exp\left(-\frac{E_a}{k_B T}\right) \tag{1}$$

where σ_0 is the pre-exponential constant, E_a is the activation energy of small polaron hopping, k_B is Boltzmann constant, and T is the absolute temperature. The values of E_a were deduced from the slope of the plot of ln (σT) versus $1000/T$. As shown in Figure 3b, good linear fittings were obtained over the whole temperature range for x = 0.625 and 0.75, and E_a was found to be 0.187 and 0.157 eV, respectively. A change in slope was observed for x = 0.5, with an E_a of 0.198 eV at the 300–600 K region and 0.167 eV at the 600–1200 K region. It is found that E_a increases with Gd content below 600 K, that is, 0.198, 0.187, and 0.157 eV for x = 0.5, 0.625, and 0.75, respectively. This may be attributed to the increasing concentration of Mn^{3+} Jahn–Teller ions which is favorable for the formation of small polarons in this temperature range [31].
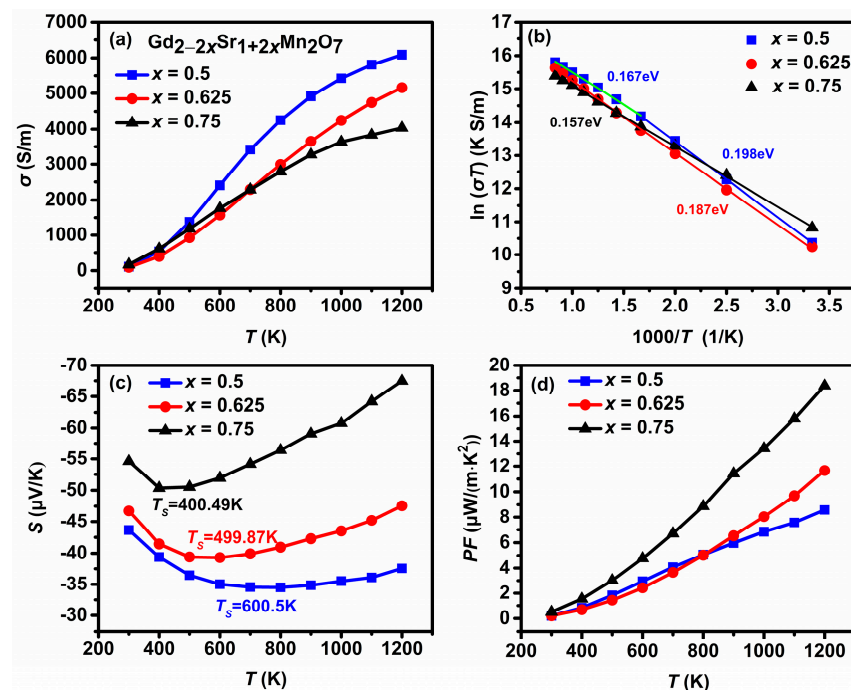

Figure 3. (a) Temperature dependence of the electrical conductivity, (b) plot of ln(σT) versus $1000/T$. The solid lines represent the fitting of the small polaron hopping model. Temperature dependence of (c) the Seebeck coefficient, and (d) the power factor for $Gd_{2-2x}Sr_{1+2x}Mn_2O_7$ (x = 0.5, 0.625, 0.75).

The values of S are negative in the whole measured temperature range as seen in Figure 3c, indicating that electrons are the dominant charge carriers. σ increases while the absolute value of S decreases with increasing Gd content due to the increase in electron carrier concentration, which is similar to those for $La_{2-2x}Ca_{1+2x}Mn_2O_7$ ($0.75 \leq x \leq 1.0$) [11], $La_{2-2x}Sr_{1+2x}Mn_2O_7$ [32], and $Gd_{1-x}Sr_xMnO_3$ ($x = 0.5, 0.6, 0.7, 0.8$) [33]. The absolute values $|S|$ at 1200 K are found to be decreased by 44% from 67.5 μV/K for $x = 0.75$ to 37.5 μV/K for $x = 0.5$. It is observed that the absolute values $|S|$ initially decrease and then increase with temperature, showing a change from a typical semiconducting behavior to a metallic or degenerate semiconducting behavior, which does not coincide with the temperature dependence of σ. The mechanism behind this phenomenon is not clear at present. The temperature Ts which are marked in Figure 3c corresponding to the minimum $|S|$ value, or the so-called metal–insulator transition temperature, was found to shift to higher temperature with increasing Gd content owing to higher electron carrier concentration. Above Ts, all the samples exhibit a metallic or degenerate semiconducting behavior arising from the enhanced scattering of electrons at high temperatures. The dependence of S on the carrier concentration n and temperature T for degenerate semiconductors can be expressed as [34]:

$$S = \frac{8\pi^2 k_B^2}{3eh^2} m^* T \left(\frac{\pi}{3n} \right)^{\frac{2}{3}} \tag{2}$$

where m^* is the effective mass of the carrier, k_B is the Boltzmann constant, e is the elementary charge, and h is Plank's constant. It is seen from Figure 3a that as T increases from room temperature to 600 K, σ increases sharply from ca. 1.0×10^2 S/m to 2.0×10^3 S/m, implying a rapid increase in electron carrier concentration n. This rapid increasing n at low temperatures is the dominant factor for the initial decrease in $|S|$ because $|S|$ is inversely proportional to the electron concentration. Then $|S|$ gradually increases with further increasing temperature for an approximately given carrier concentration. Simultaneous increases in σ and $|S|$ with increasing temperature are observed above Ts. This phenomenon was also found in $CaMnO_{3-\delta}$ [12] and $Yb_{0.1}Ca_{0.9}Mn_{1-x}Nb_xO_3$ ($x = 0.08$, 0.1) [35], and was explained by using a two-band model of S which consists of contributions from the hole (Mn^{4+}) and electron (Mn^{3+}) due to the existence of mixed-valence Mn^{3+} and Mn^{4+}. This model may be applicable to the present $Gd_{2-2x}Sr_{1+2x}Mn_2O_7$. Figure 3d shows the temperature dependence of the power factor PF. The monotonic increase in PF with temperature for all the samples is obtained due to the increases in both σ and $|S|$ at high temperatures. The PF increases with decreasing Gd content and a maximum value of 18.36 μW/(m K^2) is observed for $x = 0.75$ at 1200 K.

The measured κ was obtained using the relationship $\kappa = DC_pd$. Measurements for D and C_P were carried out from 300 to 1000 K. As seen from Figure 4a, D increases with increasing temperature and with Gd content. C_P also increases with increasing temperature, ranging from 0.46, 0.51, 0.36 J/(g K) at 300 K to 0.58, 0.69, 0.50 J/(g K) at 1000 K for $x = 0.5$, 0.625, 0.75, respectively. The values of D and C_P at 300 K are comparable to those for $La_{2-2x}Ca_{1+2x}Mn_2O_7$ in Ref. [11]. Figure 4b shows the temperature dependence of measured κ for $Gd_{2-2x}Sr_{1+2x}Mn_2O_7$ ($x = 0.5, 0.625, 0.75$). κ is lower than 2 W/(m K) over the measured temperature range. κ increases slightly with temperature and with increasing Gd content, which is constant with those for $La_{2-2x}Ca_{1+2x}Mn_2O_7$ in Ref. [11]. The measured κ consists of two contributions from phonons and electron carriers, i.e., $\kappa = \kappa_L + \kappa_e$, the lattice thermal conductivity κ_L, and the electronic thermal conductivity κ_e. κ_e can be calculated according to the Wiedemann–Franz law, $\kappa_e = L\sigma T$, where L is the Lorentz number (2.45×10^{-8} W Ω/K^2). Increasing σ is accompanied by an increase in κ_e. Temperature-dependent κ_e and κ_L are presented in Figure 4c,d. The values of κ_e are seen to be one order of magnitude smaller than those of κ_L, indicating that a significant contribution is related to the lattice vibration for the heat transport in $Gd_{2-2x}Sr_{1+2x}Mn_2O_7$. Figure 5 shows the temperature dependence of ZT. A similar trend is observed for ZT and PF. The $x = 0.75$ compound $Gd_{0.5}Sr_{2.5}Mn_2O_7$ shows better performances than the other ones due to the simultaneously enhanced S and reduced κ, with a σ of 3.6×10^3 S/m, a S of -60.8 μV/K, and a κ of 1.4 W/(m K) at 1000 K.

A maximum *ZT* of 0.01 is thus obtained for *x* = 0.75, which is comparable to that of *n*-type La$_{2-2x}$Ca$_{1+2x}$Mn$_2$O$_7$ (0.75 ≤ *x* ≤ 1.0) [11] and *p*-type Ca$_3$Co$_{2-x}$Mn$_x$O$_6$ [36]. The *ZT* value is very low for practical TE applications. These results reveal that efforts should be made to enhance σ and/or *S* through compositional and processing optimizations in order to obtain high *ZT* for these double layered manganites to be used as potential candidates for *n*-type TE materials.
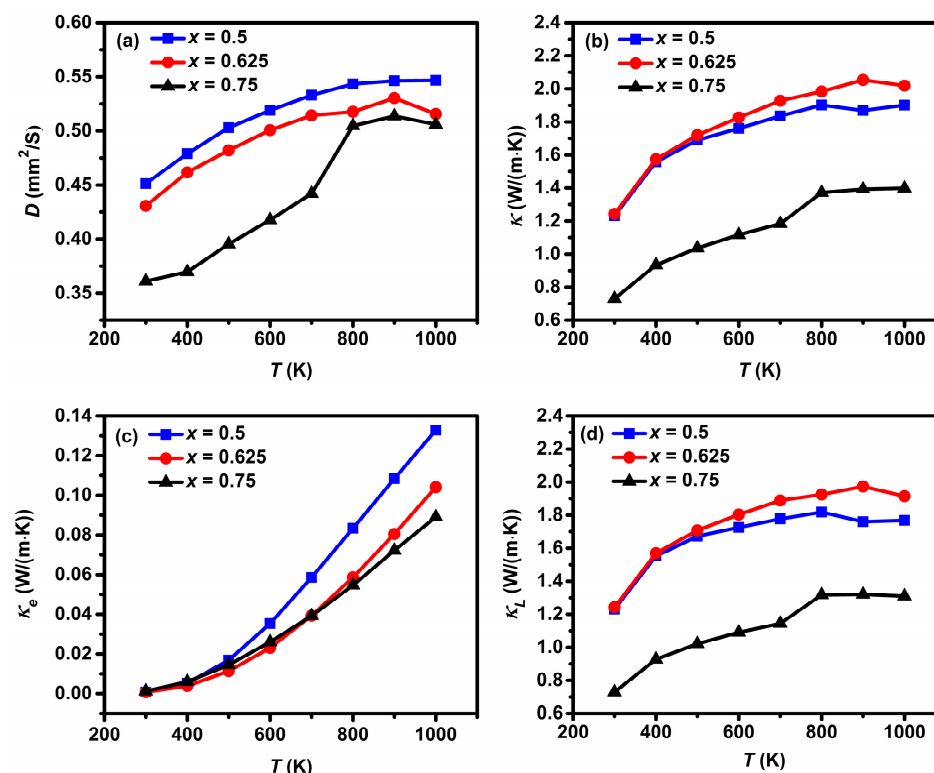
Figure 4. Temperature dependence of (**a**) the thermal diffusivity, (**b**) the measured thermal conductivity, (**c**) the electronic thermal conductivity, and (**d**) the lattice thermal conductivity for Gd$_{2-2x}$Sr$_{1+2x}$Mn$_2$O$_7$ (*x* = 0.5, 0.625, 0.75).
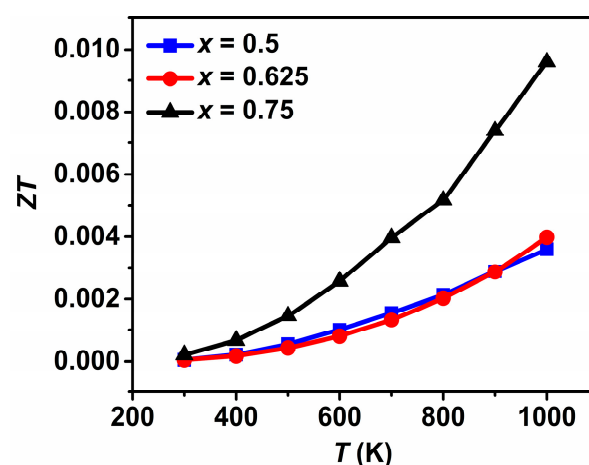
Figure 5. Temperature dependence of *ZT* for Gd$_{2-2x}$Sr$_{1+2x}$Mn$_2$O$_7$ (*x* = 0.5, 0.625, 0.75).

4. Conclusions

The structure and TE properties of Mn^{3+}/Mn^{4+} mixed-valence double-layered manganites Gd$_{2-2x}$Sr$_{1+2x}$Mn$_2$O$_7$ (*x* = 0.5, 0.625, 0.75) were studied. XRD patterns of the samples were consistent with a tetragonal Sr$_3$Ti$_2$O$_7$ type structure with space group I4/mmm

(No. 139). The Rietveld refinements indicated that the unit cell volume and the distortion in the MnO_6 octahedra increase with increasing Gd content. SEM micrographs and EDS measurements of all the samples show dense and uniform microstructures. All the samples are *n*-type semiconductors, and σ can be fitted well by the small polaron hopping model in the whole temperature range. With increasing Gd content, σ increases while $|S|$ decreases due to the increasing electron carrier concentration. It is found that the absolute values $|S|$ initially decrease and then increase with temperature, and both σ and $|S|$ increase with temperature approximately above 600 K, resulting in a monotonic increase in *PF*. These phenomena are interesting, and the physical mechanisms are worthy of further study. κ increases with increasing Gd content, and is lower than 2 W/(m K) over the temperature range of 300–1000 K. A maximum *ZT* of 0.01 is obtained for $x = 0.75$ at 1000 K. Although the *ZT* of $Gd_{2-2x}Sr_{1+2x}Mn_2O_7$ does not yet reach the performance required for practical TE materials, the present study sheds light on their electrical and thermal transport properties and the relevant mechanisms and lays a foundation for seeking new applications for these double-layered manganites.

Author Contributions: Methodology, N.Q. and Y.P.; formal analysis, N.Q. and Y.P.; investigation, N.Q.; resources, X.C. and Z.X.; writing—original draft preparation, N.Q.; writing—review and editing, J.Y.; supervision, J.Y.; project administration, X.C. and J.Y.; funding acquisition, X.C. and J.Y. All authors have read and agreed to the published version of the manuscript.

Institutional Review Board Statement: Not applicable.

Informed Consent Statement: Not applicable.

Data Availability Statement: Data are contained within the article.

Conflicts of Interest: The authors declare no conflict of interest.

References

1. Terasaki, I.; Sasago, Y.; Uchinokura, K. Large thermoelectric power in $NaCo_2O_4$ single crystals. *Phys. Rev. B* **1997**, *56*, R12685–R12687. [CrossRef]
2. Fergus, J.W. Oxide materials for high temperature thermoelectric energy conversion. *J. Eur. Ceram. Soc.* **2012**, *32*, 525–540. [CrossRef]
3. Yin, Y.N.; Tudu, B.; Tiwari, A. Recent advances in oxide thermoelectric materials and modules. *Vacuum* **2017**, *146*, 356–374. [CrossRef]
4. Zhao, L.-D.; He, J.; Berardan, D.; Lin, Y.; Li, J.-F.; Nan, C.-W.; Dragoe, N. BiCuSeO oxyselenides: New promising thermoelectric materials. *Energy Environ. Sci.* **2014**, *7*, 2900–2924. [CrossRef]
5. Megha, A.; Sourav, J.S.; Mani, R.; Tanmoy, M. High performance (ZT>1) n-type oxide thermoelectric composites from earth abundant materials. *Nano Energy* **2021**, *84*, 105905. [CrossRef]
6. Wang, H.; Su, W.; Liu, J.; Wang, C. Recent development of n-type perovskite thermoelectrics. *J. Mater.* **2016**, *2*, 225–236. [CrossRef]
7. Walia, S.; Balendhran, S.; Nili, H.; Zhuiykov, S.; Rosengarten, G.; Wang, Q.H.; Bhaskaran, M.; Sriram, S.; Strano, M.S.; Kalantar-zadeh, K. Transition metal oxides—Thermoelectric properties. *Prog. Mater Sci.* **2013**, *58*, 1443–1489. [CrossRef]
8. Kimura, T.; Tokura, Y. Layered Magnetic Manganites. *Annu. Rev. Mater. Sci.* **2000**, *30*, 451–474. [CrossRef]
9. Dawley, N.M.; Pek, E.K.; Lee, C.-H.; Ragasa, E.J.; Xiong, X.; Lee, K.; Phillpot, S.R.; Chernatynskiy, A.V.; Cahill, D.G.; Schlom, D.G. Thermal conductivity of the n = 1–5 and 10 members of the $(SrTiO_3)nSrO$ Ruddlesden–Popper superlattices. *Appl. Phys. Lett.* **2021**, *118*, 091904. [CrossRef]
10. Wang, Y.F.; Lee, K.H.; Ohta, H.; Koumoto, K. Fabrication and thermoelectric properties of heavily rare-earth metal-doped $SrO(SrTiO_3)_n$ (n=1, 2) ceramics. *Ceram. Int.* **2008**, *34*, 849–852. [CrossRef]
11. Toyoda, T.; Sasaki, N.; Shimada, K.; Okube, M.; Sasaki, S. High-Temperature Thermoelectric Property of Layered $La_{2-2x}Ca_{1+2x}Mn_2O_7$ Manganites ($0.75 \leq x \leq 1.0$). *Jpn. J. Appl. Phys.* **2011**, *50*, 041101. [CrossRef]
12. Liu, C.-J.; Bhaskar, A.; Yuan, J.J. High-temperature transport properties of $Ca_{0.98}RE_{0.02}MnO_{3-\delta}$ (RE=Sm, Gd, and Dy). *Appl. Phys. Lett.* **2011**, *98*, 214101. [CrossRef]
13. Sun, R.R.; Qin, X.Y.; Li, L.L.; Li, D.; Zhang, J.; Zhang, Y.S.; Tang, C.J. The effects of elements doping on transport and thermoelectric properties of $Sr_3Ti_2O_7$. *J. Phys. Chem. Solids* **2014**, *75*, 629–637. [CrossRef]
14. Wang, Y.F.; Lee, K.H.; Hyuga, H.; Kita, H.; Ohta, H.; Koumoto, K. Enhancement of thermoelectric performance in rare earth-doped $Sr_3Ti_2O_7$ by symmetry restoration of TiO_6 octahedra. *J. Electroceram.* **2010**, *24*, 76–82. [CrossRef]

15. Mitchell, J.F.; Argyriou, D.N.; Berger, A.; Gray, K.E.; Osborn, R.; Welp, U. Spin, Charge, and Lattice States in Layered Magnetoresistive Oxides. *J. Phys. Chem. B* **2001**, *105*, 10731–10745. [CrossRef]

16. Zhang, J.; Wang, F.; Zhang, P.; Sun, X.; Yan, Q. Magnetic and electric properties of layered perovskites $Nd_{2-2x}Sr_{1+2x}Mn_2O_7$ (x=0.3–0.5). *J. Magn. Magn. Mater.* **1998**, *190*, 166–170. [CrossRef]

17. Moritomo, Y.; Asamitsu, A.; Kuwahara, H.; Tokura, Y. Giant magnetoresistance of manganese oxides with a layered perovskite structure. *Nature* **1996**, *380*, 141–144. [CrossRef]

18. Kimura, T.; Tomioka, Y.; Kuwahara, H.; Asamitsu, A.; Tamura, M.; Tokura, Y. Interplane Tunneling Magnetoresistance in a Layered Manganite Crystal. *Science* **1996**, *274*, 1698–1701. [CrossRef]

19. Hur, N.H.; Kim, J.-T.; Yoo, K.H.; Park, Y.K.; Park, J.-C. Effect of lanthanide ions on the magnetotransport properties in layered $Sr_{1.6}R_{1.4}Mn_2O_7$ (R=La, Pr, Nd, Gd). *Phys. Rev. B* **1998**, *57*, 10740–10744. [CrossRef]

20. Asano, H.; Hayakawa, J.; Matsui, M. Two-dimensional ferromagnetic ordering and magnetoresistance in the layered perovskite $La_{2-2x}Ca_{1+2x}Mn_2O_7$. *Phys. Rev. B* **1997**, *56*, 5395–5403. [CrossRef]

21. Battle, P.D.; Green, M.A.; Laskey, N.S.; Kasmir, N.; Millburn, J.E.; Spring, L.E.; Sullivan, S.P.; Rosseinsky, M.J.; Vente, J.F. Control of electronic properties by lanthanide size and manganese oxidation state in the Mn^{III}/Mn^{IV} Ruddlesden-Popper phases $Ln_{2-x}Sr_{1+x}Mn_2O_7$. *J. Mater. Chem.* **1997**, *7*, 977–988. [CrossRef]

22. He, L.; Qin, N.; Wei, J.; Li, M.; Song, Y.; Yan, J. Metastable phase diagram of the Gd_2O_3–SrO–CoO_x ternary system. *Int. J. Mater. Res.* **2022**, *113*, 508–519. [CrossRef]

23. Wei, J.X.; Yin, Y.; Yan, J.L. Structural and thermoelectric properties of $Gd_xSr_{2-x}CoO_4$ layered perovskites. *Ceram. Int.* **2021**, *47*, 19835–19842. [CrossRef]

24. Argyriou, D.N.; Mitchell, J.F.; Potter, C.D.; Bader, S.D.; Kleb, R.; Jorgensen, J.D. Unconventional magnetostriction in layered $La_{1.2}Sr_{1.8}Mn_2O_7$: Evidence for spin-lattice coupling above T_C. *Phys. Rev. B* **1997**, *55*, R11965–R11968. [CrossRef]

25. Kumar, B.; Tiwari, J.K.; Chauhan, H.C.; Ghosh, S. Multiple magnetic phase transitions with different universality classes in bilayer $La_{1.4}Sr_{1.6}Mn_2O_7$ manganite. *Sci. Rep.* **2021**, *11*, 21184. [CrossRef]

26. Rodríguez-Carvajal, J. Recent advances in magnetic structure determination by neutron powder diffraction. *Physica B* **1993**, *192*, 55–69. [CrossRef]

27. Battle, P.D.; Green, M.A.; Laskey, N.S.; Millburn, J.E.; Murphy, L.; Rosseinsky, M.J.; Sullivan, S.P.; Vente, J.F. Layered Ruddlesden-Popper manganese oxides: Synthesis and cation ordering. *Chem. Mater.* **1997**, *9*, 552–559. [CrossRef]

28. Ruck, K.; Dorr, K.; Nenkov, K.; Muller, K.H.; Krabbes, G.; Schupp, B.; Khristov, M. Magnetic and transport properties of $Nd_{0.2}La_{1.8-2x}Sr_{1+2x}Mn_2O_7$ (x=0.5, 0.4, 0.3) and $La_{1.5}Sr_{1.5}Mn_2O_7$. *J. Phys. Condens. Matter* **2001**, *13*, 1571–1583. [CrossRef]

29. Zhu, Y.; Wang, C.; Su, W.; Li, J.; Liu, J.; Du, Y.; Mei, L. High-temperature thermoelectric performance of $Ca_{0.96}Dy_{0.02}RE_{0.02}MnO_3$ ceramics (RE=Ho, Er, Tm). *Ceram. Int.* **2014**, *40*, 15531–15536. [CrossRef]

30. Nag, A.; Shubha, V. Oxide Thermoelectric Materials: A Structure–Property Relationship. *J. Electron. Mater.* **2014**, *43*, 962–977. [CrossRef]

31. Lan, J.; Lin, Y.-H.; Fang, H.; Mei, A.; Nan, C.-W.; Liu, Y.; Xu, S.; Peters, M. High-Temperature Thermoelectric Behaviors of Fine-Grained Gd-Doped $CaMnO_3$ Ceramics. *J. Am. Ceram. Soc.* **2010**, *93*, 2121–2124. [CrossRef]

32. Nakamae, S.; Colson, D.; Forget, A.; Legros, I.; Marucco, J.F.; Ayache, C.; Ocio, M. Thermoelectric power of hole-doped manganites: $La_{2-2x}Sr_{1+2x}Mn_2O_7$ ($0.3 \leq x \leq 0.5$). *Phys. Rev. B* **2001**, *63*, 092407. [CrossRef]

33. Tanwar, K.; Anjum, F.; Shukla, A.K.; Maiti, T. Role of structural distortion on thermoelectric aspects of heavily Sr^{2+} doped $GdMnO_3$. *J. Appl. Phys.* **2018**, *124*, 094902. [CrossRef]

34. Cutler, M.; Leavy, J.F.; Fitzpatrick, R.L. Electronic Transport in Semimetallic Cerium Sulfide. *Phys. Rev.* **1964**, *133*, A1143–A1152. [CrossRef]

35. Wang, C.; Shi, L.; Xu, X.; Zhou, S.; Zhao, J.; Guo, Y.; Liu, H.; He, L.; Cai, X.; Xu, G. High-temperature thermoelectric characteristics of B-site substituted $Yb_{0.1}Ca_{0.9}Mn_{1-x}Nb_xO_3$ system ($0 \leq x \leq 0.1$). *Appl. Phys. A* **2013**, *112*, 1003–1009. [CrossRef]

36. Kanas, N.; Singh, S.P.; Rotan, M.; Desissa, T.D.; Grande, T.; Wiik, K.; Norby, T.; Einarsrud, M.-A. Thermoelectric Properties of $Ca_3Co_{2-x}Mn_xO_6$ (x = 0.05, 0.2, 0.5, 0.75, and 1). *Materials* **2019**, *12*, 497. [CrossRef]